ACS APPLIED MATERIALS & INTERFACES

Research Article

www.acsami.org

Cellulose Nanocrystals vs. Cellulose Nanofibrils: A Comparative Study on Their Microstructures and Effects as Polymer Reinforcing Agents

Xuezhu Xu,[†,‡] Fei Liu,[†] Long Jiang,*[,†] J. Y. Zhu,[§] Darrin Haagenson,[⊥] and Dennis P. Wiesenborn[⊥]

[†]Department of Mechanical Engineering, [‡]Program of Materials and Nanotechnology, [⊥]Department of Agricultural and Biosystems Engineering, North Dakota State University,Fargo, North Dakota 58108, United States

[§]Forest Products Laboratory, USDA Forest Service, Madison, Wisconson 53726, United States

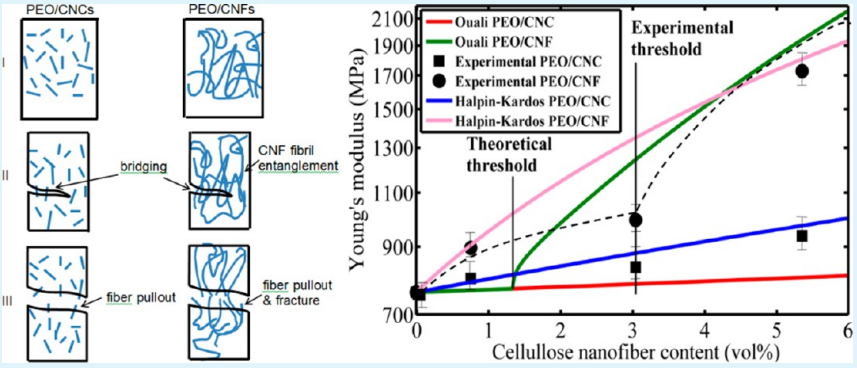

ABSTRACT: Both cellulose nanocrystals (CNCs) and cellulose nanofibrils (CNFs) are nanoscale cellulose fibers that have shown reinforcing effects in polymer nanocomposites. CNCs and CNFs are different in shape, size and composition. This study systematically compared their morphologies, crystalline structure, dispersion properties in polyethylene oxide (PEO) matrix, interactions with matrix, and the resulting reinforcing effects on the matrix polymer. Transparent PEO/CNC and PEO/CNF nanocomposites comprising up to 10 wt % nanofibers were obtained via solution casting. Scanning electron microscopy (SEM), wide-angle X-ray diffraction (WXRD), transmission electron microscopy (TEM), Fourier transform infrared spectroscopy (FTIR), dynamic mechanical analyzer (DMA), and tensile testing were used to examine the above-mentioned properties of nanocellulose fibers and composites. At the same nanocellulose concentration, CNFs led to higher strength and modulus than did CNCs due to CNFs' larger aspect ratio and fiber entanglement, but lower strain-at-failure because of their relatively large fiber agglomerates. The Halpin-Kardos and Ouali models were used to simulate the modulus of the composites and good agreements were found between the predicted and experimental values. This type of systematic comparative study can help to develop the criteria for selecting proper nanocellulose as a biobased nano-reinforcement material in polymer nanocomposites.

KEYWORDS: *cellulose nanocrystals, cellulose nanofibrils, polymer nanocomposites, reinforcing mechanism, Kapin−Kardos model, percolation theory*

INTRODUCTION

Biobased materials have attracted immense research intrest in recent years because of their great potential for producing a variety of high-value products with low impact on the environment. Both cellulose nanocrystals (CNCs) and cellulose nanofibrils (CNFs) can be isolated from plant cell walls. The abundant availability of plant biomass and the superior mechanical properties of cellulose made nanocellulose including CNCs and CNFs a desirable reinforcing material for polymer nanocomposites.[1] Cellulose is a linear chain polysaccharide consisting of repeated β-(1→4)-D-glucopyranose units. Hydroxyl groups are abundant on CNC and CNF surfaces, allowing potential hydrogen bonding and surface modifications.

CNCs (also called cellulose nanowhiskers) are needlelike cellulose crystals of 10−20 nm in width and several hundred nanometers in length. They are produced from various biological sources (e.g., bleached wood pulp, cotton, manila, tunicin, bacteria, etc.) often by strong acid hydrolysis.[2,3] Acid treatments remove noncellulose components and most amorphous cellulose from the source materials and produce high purity cellulose crystals. Therefore, CNCs are highly crystalline. CNCs have been incorporated as reinforcing agents into a wide range of polymer matrices such as poly(oxyethylene), poly(vinyl alcohol), natural rubber, starch, and polyurethane.[4−12] CNFs form long flexible fiber networks with a fibril diameter similar to or larger than CNCs. CNFs can be produced by TEMPO-mediated oxidation (2,2,6,6,-tetrame-

Received: November 8, 2012
Accepted: March 22, 2013
Published: March 22, 2013

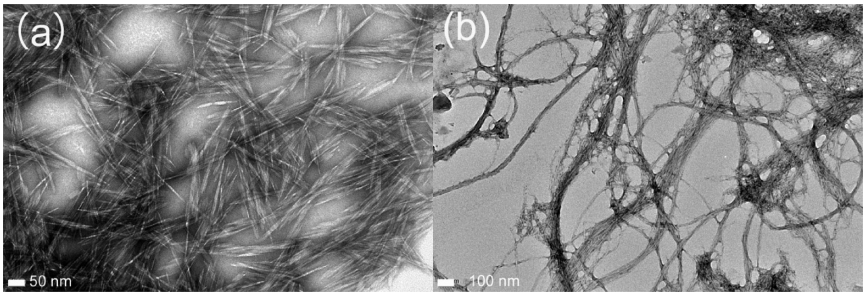

Figure 1. High-resolution TEM images of (a) CNCs and (b) CNFs.

thylpipelidine-1-oxyl radical), multi-pass high-pressure homogenization, enzymatic hydrolysis[13,14] or direct mechanical fibrillation.[15] The morphologies and dimensions of CNFs can vary substantially, depending on the degrees of fibrilation and any pretreatment involved. CNFs contain amorphous cellulose and are not as highly crystalline as CNCs. Numerous studies have been carried out using various cellulosic fibers or fibrils for polymer reinforment.[16−26] These studies indicate that fibrils with smaller diameters and longer lengths exhibit stronger reinforcing effect. For example, Siqueira et al. compared the effects of CNCs and microfibrillated cellulose (MFC, average diameter ca. 50 nm) on the crystallization and mechanical properties of polycaprolactone (PCL) matrix. The authors find that CNCs act as a better nucleation agent for PCL than MFC because of the latter's entanglement and confinement effect which restricts the growth of PCL crystallites.[23] MFC imparts higher modulus to the composites than do CNCs for the same reason. However, MFC and CNCs were both shown to decrease the strength and strain-at-failure of PCL, with higher fiber contents leading to larger decrease.

Both MFC and CNFs have large aspect ratios and are expected to have some similarities as reinforcent materials; however, extended mechanical fibrillation imparts CNFs complex fibril networks and much thinner fibrils compared with MFC. It is of great interest to compare the performance of CNFs and CNCs as reinforcing materials for nanocomposites. In this study, we compared the effect of CNCs and CNFs on the mechanical and thermal dynamic properties of PEO to understand the contributions of their morphologies and dispersions to the properties of PEO nanocomposites. Experimentally measured mechanical properties were compared with theoretical predictions on the basis of two mechanical models and correlated with the microstructures of the nanocomposites. Remarkable differences in the reinforcing effects between CNCs and CNFs were demonstrated and a microstructural explanation was provided. Different forms of cellulose nanofibers as reinforcement agents in polymer nanocomposites have been intensively studied and great potential has been shown for their industrial applications. In spite of all previous studies, a greater clarity is needed on the reinforcing effects of different cellulose nanofibers. The results from this study show clear distinctions between short rigid CNCs and long relatively tough CNFs in terms of their reinforcing effects and mechanisms, thus providing a practical guidance for the development of polymer nanocomposites containing cellulose nanofibers. Novel applications of PEO/cellulose nanocomposites as water absorption and retention materials[27] and as solid−solid phase change materials for energy storage[28] can also benefit from this study.

MATERIALS AND METHODS

CNCs and CNFs derived from bleached dry lap eucalyptus pulp were kindly provided by the USDA Forest Service Lab. Their methods of production have been detailed elsewhere.[15,29] Briefly, CNCs were produced by sulfuric acid hydrolysis followed by repeated centrifugation[29] whereas CNFs were produced through a multi-pass high pressure grinding process using a SuperMassColloider (MKZA6-2, Masuko Sangyo Co., Ltd, Japan).[15] The as-received CNCs and CNFs were in the forms of 5.7 wt % suspension and 1.8 wt % gel (both in water), respectively. PEO with a viscosity average molecular weight (M_v) of 1 000 000 was purchased from Sigma-Aldrich. PEO/CNC and PEO/CNF nanocomposite films were prepared by solution casting. PEO was first dissolved in deionized water to make a 4 wt % solution. Various amounts of CNC suspension or CNF gel were added to the solution to make mixtures comprising 0, 1, 4, 7, and 10 wt % of CNCs or CNFs (based on PEO solid weight). The mixtures were first homogenized using a homogenizer (IKA T25 digital Ultra-Turrax) at 100 rpm for 5 minutes at room temperature and then stirred using a magnetic stirrer at approximately 100 rpm at 60 °C for 12 h. Nanocomposite films were obtained by casting the mixtures in glass Petri dishes and drying the casts in a vacuum oven at 80 °C for approximately 5 h.

TEM was used to study the morphology of CNC and CNF fibers and their dispersion states in PEO matrix. TEM imaging was conducted on a JEOL JEM-2100 Lab6 operating at 200 kV. To prepare the CNC and CNF samples for TEM study, the CNC suspension and CNF gel were both diluted with distilled water. Specifically, 0.5 ml of the 5.7% CNC suspension was diluted 100 times in distilled water. A drop (accurate measurements were not allowed due to the high viscosity of the gel) of the 1.8% CNF gel was added to 0.5 mL of distilled water and manually stirred. A drop of each diluted sample was placed onto 300 mesh Formvar coated copper grids. Extra liquid was wicked off with filter paper. Samples were allowed to dry at room temperature and finally stained with 1% phosphotungstic acid (PTA) or iodine vapor to produce additional contrast. To study dispersion of CNCs and CNFs in the PEO matrix, drops of mixture solutions were deposited onto carbon-coated copper grids and allowed to dry at room temperature. The specimens were also stained with iodine vapor to enhance image contrast.

Wide-angle X-ray diffraction (WAXD) measurements were performed using an X-ray powder diffractometer (Philips X'Pert MPD) operating at 45 kV and 40 mA with a Cu Kα X-ray source. Pure dry CNC and CNF films (prepared by vacuum drying of the as-received dispersion and gel) were scanned from 2.5−60° at a scanning speed of 0.05°/s.

Dynamic mechanical analysis (DMA) of composite films was conducted using a DMA Q800-0790 (TA Instruments) equipped with a film tension clamp. Test samples (12.74 × 6.29 mm^2) were prepared using a die cutter. Tests were run from -100 to 20 °C (T_g of PEO: −48 °C) at a rate of 3°C/min. Oscillation amplitude of 20 μm (within linear range) and a preload force of 0.01 N were applied on all samples. At least three repeats were tested for each sample.

Differential scanning calorimetry (DSC) tests were conducted using a Q1000 from TA Instruments. Samples (2−6 mg each) were sealed in

aluminum pans, tested under continuous nitrogen flow (50.0 mL/min), and scanned from 25 to 100 °C at a ramp rate of 10 °C/min.

A Fourier transform infrared (FTIR) spectrometer (Nicolet 6700) from Thermo Scientific was used to examine interactions between the nanofibers and the PEO matrix. Thirty-two repetitive scans with a resolution of 0.482 cm^{-1} were performed on each sample.

Tensile tests were conducted using an Instron 5545 Tensile tester equipped with a 100 N load cell. Tensile specimens were cut using a dumbbell die with a width and length of 2 and 20 mm (narrow section of the die), respectively. The speed of testing was 20 cm/min. Ten specimens were measured for each sample to get an average value.

RESULTS AND DISCUSSION

Morphology and Crystalline Structure of CNCs and CNFs. CNCs and CNFs show substantially different shapes and sizes in TEM micrographs (Figure 1). CNCs present a simple needle-like structure with an average length (L) of 151 ± 39 nm, a width (w) of 19 ± 5 nm, and a resultant aspect ratio of L/w of 8 (based on 100 measurements from 5 micrographs). CNFs exhibit a complex, highly-entangled, web-like structure. Twisted/untwisted, curled/straight, and entangled/separate nanofibrils and their bundles with diameters ranging from 6 to 100 nm in diameter can be identified from the micrograph. The highly entangled structure of CNFs significantly increases resistance to flow and results in gel-like behavior of the as-received CNF sample. By contrast, the as-received CNC suspension shows much lower viscosity than the CNF sample even at higher fiber concentration (5.7 vs. 1.8 wt %) because of the former's low aspect ratio and lack of entanglement. Given CNFs' complex network morphology, it was difficult to measure the length and diameter of individual CNF with high accuracy. On the basis of the individual CNF and bundles that could be clearly identified from the micrographs, CNFs show an average width and length of 20 ± 14 nm and 1030 ± 334 nm (based on 50 measurements from 4 micrographs), resulting in an aspect ratio of $L/w \geq 52$. Admittedly, the actual aspect ratio of CNFs in the composites might vary because of the existence of CNF bundles.

X-ray diffraction patterns of CNCs and CNFs are compared in Figure 2. The XRD results including peak angle (2θ), d-spacing, full width at half maximum (FWHM), average crystal size (thickness) in the direction normal to the reflecting plane (L) and crystallinity index (CI) are summarized in Table 1. The crystal size was determined by the Scherrer equation[30]

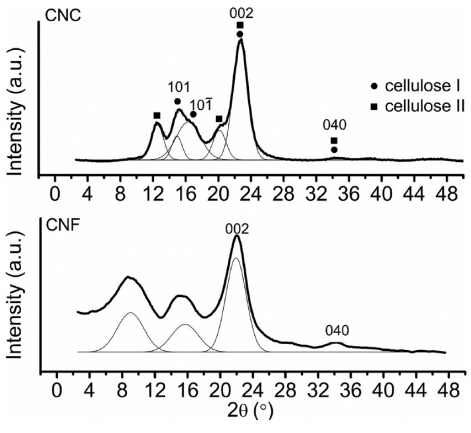

Figure 2. Wide-angle X-ray diffraction patterns of CNCs and CNFs.

Table 1. XRD Results of Pure CNCs and CNFs

	2θ	d (Å)	FWHM	L (Å)	CI (%) (Segal)	CI (%) (Jade)
CNCs	12.5	7.1	0.996	35	81.0	95
	15.1	5.8	1.033	27		
	17.5	5.2	1.029	78		
	20.1	4.4	1.488	54		
	22.7	3.9	1.102	38		
	34.3	2.6	8.146	10		
CNFs	9.2	9.6	0.964	13	64.4	39
	14.9	6.0	1.370	15		
	22.4	4.0	1.135	29		
	33.9	2.6	1.984	42		

$$\mathrm{FWHM}(2\theta) = \frac{K\lambda}{L\cos\theta} \quad (1)$$

Where K is the Scherrer constant (0.89) and λ is the X-ray wavelength. CI of CNCs and CNFs can be determined based on XRD results using several different methods.[31] Segal method allows rapid comparison of cellulose crystallinity and is commonly used in the paper industry[32]

$$\mathrm{CI} = \frac{I_{002} - I_{\mathrm{amorphous}}}{I_{002}} \quad (2)$$

Where I_{002} is the maximum intensity of the (002) diffraction and I is the intensity of amorphous diffraction, which is taken at 2θ angle between (002) and (101) peaks where the intensity is at a minimum. The second method separates amorphous and crystalline diffractions and calculates the ratio of the crystalline diffraction to the overall diffraction as CI using MDI Jade 6.5 software (Materials Data, Inc.).[33]

CNCs show diffraction peaks at 15.1, 17.5, 22.7, and 34.3°, representing cellulose I crystal planes (101), (10$\bar{1}$), (002), and (040), respectively.[25] Diffractions from cellulose II are also present in the CNC pattern at angles of 12.5, 20.1, 22.7, and 34.3°.[34] The coexistence of cellulose I and cellulose II in CNCs is attributed to the alkali pulping and acid hydrolysis processes that CNCs experience during production. Alkali and acid treatments to natural fibers transform cellulose I to cellulose II.[34,35] XRD results of CNFs are surprisingly scarce in the literature. This study found that CNFs showed broadened and merged peaks, which also shifted to lower angles. Millett et al. found that the diffraction peaks of ball milled natural fibers were also shifted to lower angles with increasing milling time because of the superposition of the broadened crystalline diffraction peaks upon increasingly strong amorphous diffractions.[35] This is also the case in this study. The high pressure mechanical grinding used in CNF manufacturing could deform or even completely destruct cellulose crystals, leading to broadened and shifted diffraction peaks.[25]

Crystallinity index (CI) values determined by both the Segal method and Jade software show that CNCs have higher crystallinity than CNFs, which is in agreement with the microstructures of the two nanofibers. However, the two methods show large differences in CI values, with the Jade software producing a larger value for CNCs and a lower value for CNFs. The differences are attributed to Segal method's over-simplicity and the resultant inaccurate results.[31]

Dispersion and Percolation of CNCs and CNFs in PEO. The degree of transparency of the nanocomposite films indicates the status of dispersion of CNCs and CNFs. As

dx.doi.org/10.1021/am302624t | ACS Appl. Mater. Interfaces 2013, 5, 2999−3009

shown in Figure 3, the PEO/CNC film was nearly optically transparent while the PEO/CNF film was translucent,

Figure 3. PEO/CNF and PEO/CNC nanocomposite films at room temperature. CNF and CNC concentration: 7%.

indicating CNCs' smaller nanoparticle sizes and better dispersion. A closer observation showed that PEO/CNCs exhibits higher transparency than does PEO/CNFs, most likely due to CNCs' smaller sizes and lack of agglomeration and entanglement. This property is advantageous to optical applications where several common nanocomposites (e.g., carbon and clay naocomposites) can't be used because of their lack of transparency.

CNCs are seen homogeneously dispersed in the PEO matrix without signs of fiber aggregation (Figure 4a). No obvious CNC percolation network is found in the composites. At a higher magnification (Figure 4b), elementary cellulose crystallites with multi-layer structures are clearly identified. The structures showed an overall average thickness of approximately 3.6 nm, an average dark layer thickness of 0.386 nm, and an average light layer thickness of 0.173 nm. The thickness of one dark layer and one light layer comprised a d-spacing of 0.559 nm. Very recently, Liu et al. showed a similar structure and indicated that the structure represents cellulose crystal lattice fringes.[26] The cellulose elementary crystallites were reported to have a cross-sectional size of 3−5 nm,[36] which matches the measured overall thickness of the multilayer structure in this study. The larger average width of CNCs than the multilayer structure thickness (19 nm compared to 3.6 nm) indicates that most CNCs contain more than one laterally aggregated elementary cellulose crystallite.[37]

CNFs maintained their entangled fibril structure in the PEO matrix (Figure 5). An average fibril width of 20 nm was estimated based on the micrographs. The grinding process produced CNFs with a wide width distribution, ranging from a single elemental fibril (~6 nm) to nanofibrils (~100 nm) as shown in Figure 1b. CNF fibril length also varied substantially, with both long (Figure 5a, d) and short (Figure 5b,c) fibrils clearly seen. Additionally, CNF entanglements and network structure throughout the matrix are evident in the Figures. These entanglements play an important role in the force transferring from matrix to fibrils and from fibrils to fibrils. CNF aggregates can also be seen in Figure 5a,d.

FT-IR. FT-IR was used to evaluate the hydrogen bonding interaction between CNCs (or CNFs) and the PEO matrix. Figure 6 shows the FT-IR absorption spectra in the hydroxyl stretching region (3500−3000 cm^{-1}). Pure PEO exhibits a broad stretching peak centered at 3435.5 cm^{-1}. The stretching peaks for pure CNCs and CNFs are much sharper and stronger, indicating higher densities of the hydroxyl groups on the surfaces of CNCs and CNFs. Four individual minor peaks are identified from CNCs' spectrum, i.e., 3486.0, 3439.4, 3331.1, and 3287.1 cm^{-1}. The former two peaks are ascribed to intramolecular hydrogen bonding and the latter two to intermolecular hydrogen bonding.[38,39] These minor peaks are not as obvious on the spectrum of CNFs. Instead, a bump at 3427.8 cm^{-1} and two weak peaks at 3283.7 and 3323.3 cm^{-1} can be seen in Figure 6. For both PEO/CNC and PEO/CNF composites, the stretching peaks shift to higher frequencies with increasing CNC or CNF contents, indicating the effects of the cellulose nanofibers on the PEO matrix through hydrogen bonding. For example, the 3331.1 cm^{-1} peak of pure CNCs shift to 3336.3 and 3338.3 cm^{-1} for the 7 and 10 wt % PEO/CNC composites, respectively. Similarly, the 3283.7 cm^{-1} peak of pure CNFs shifts to 3340.1 and 3343.1 cm^{-1} for the PEO/CNF composites. The larger shift on the PEO/CNF composites may indicate stronger hydrogen bonding between PEO and CNFs than between PEO and CNCs. Many hydroxyl groups on CNCs were replaced with SO_3^{-1} during sulfuric acid hydrolysis and thus the potential for hydrogen bonding is reduced. The significant decrease of the intensity on the 3287.1 cm^{-1} (for CNCs) and 3323.3 cm^{-1} (for CNFs) peaks also shows their strong interactions with the PEO matrix.

The peak at 957 cm^{-1} on the spectrum of pure PEO is attributed to CH_2 rocking and influenced by C−O−C stretching (Figure 7).[40] Neither CNCs nor CNFs show similar peaks at this region. However, the presence of CNCs or CNFs in the PEO/CNC or PEO/CNF nanocomposites upshifts the peak by approximate 5 cm^{-1}. Changes in the intensity ratio of 1143 cm^{-1} to 1096 cm^{-1} are also observed. The two peaks belong to the characteristic triplet of PEO (i.e., 1143, 1096, and 1059 cm^{-1}), which is assigned to C−O−C stretching.[41] The intensities and frequencies of the triplet are influenced by the crystallinity of PEO and the intermolecular interactions (e.g., hydrogen bonding) between C−O−C and other materials.[42,43] C−O−C is a proton acceptor and can form hydrogen bonding

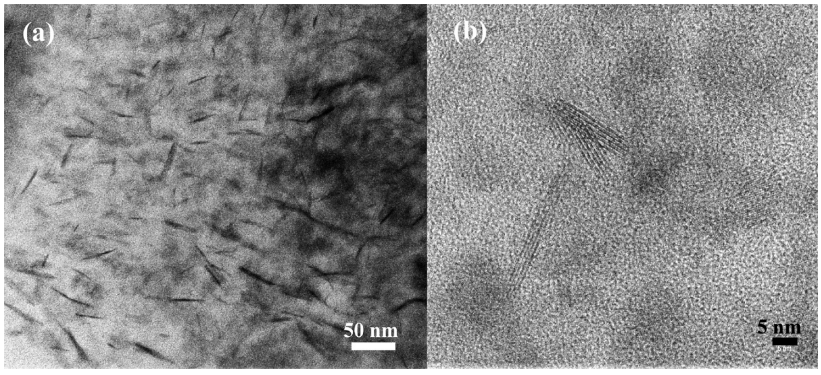

Figure 4. TEM images of (a) PEO/CNC (7%) nanocomposite film and (b) CNC crystallites.

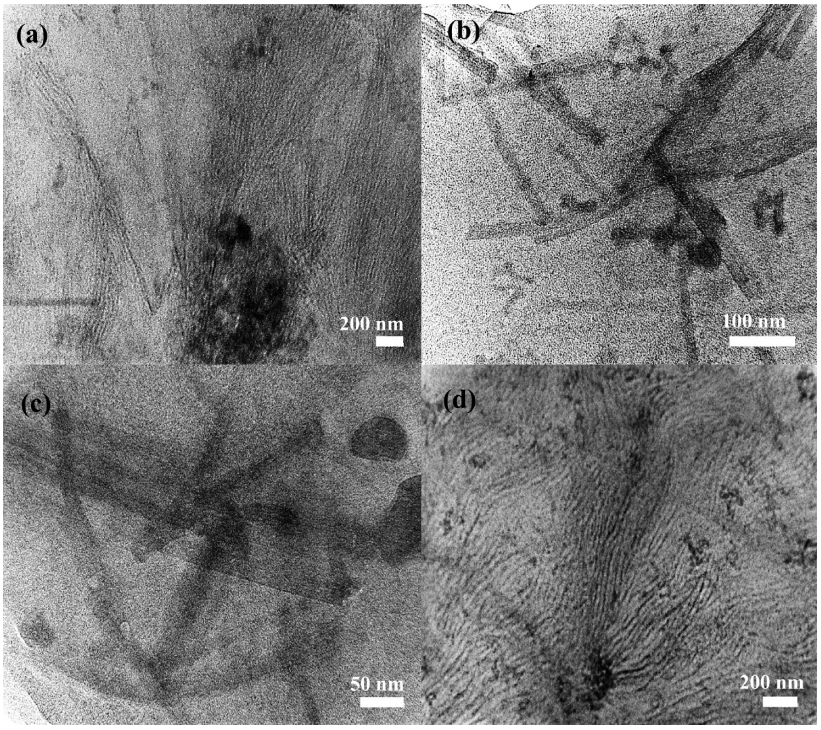

Figure 5. TEM images of (a–c) PEO/7 wt % CNFs and (d) PEO/10 wt % CNFs.

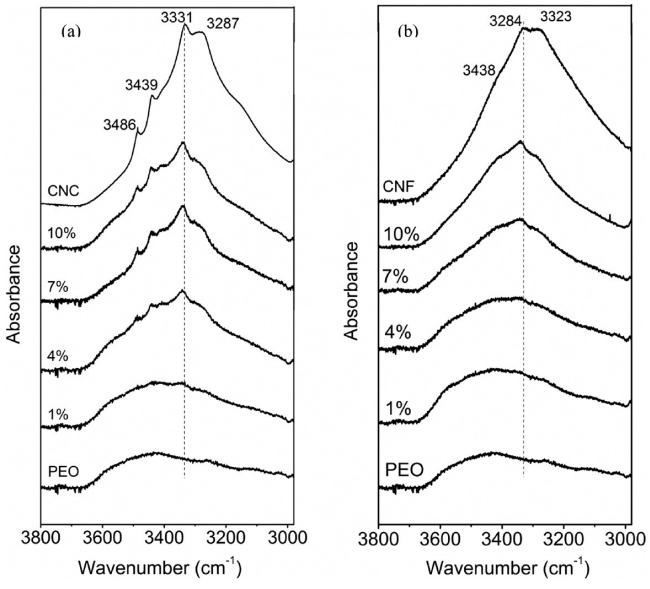

Figure 6. FT-IR spectra in the region of hydroxyl stretching for (a) PEO/CNC and (b) PEO/CNF composites with various nanofiber contents.

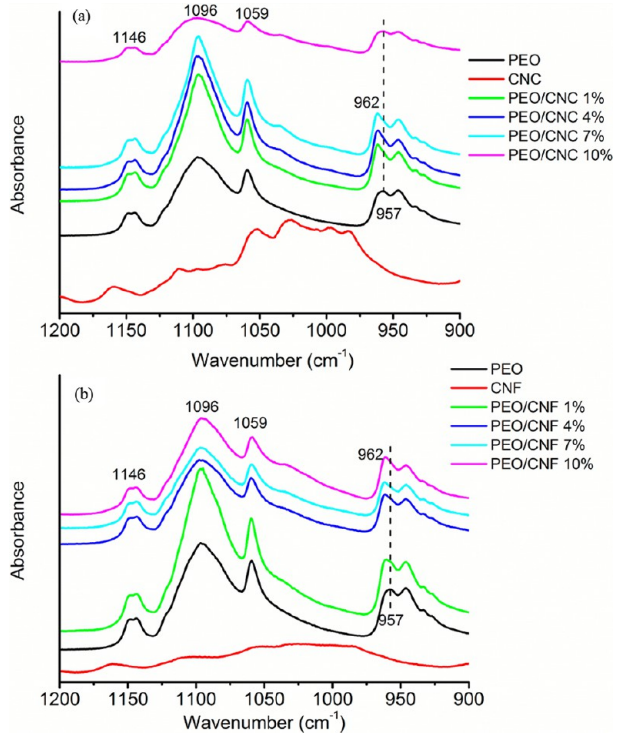

Figure 7. FT-IR spectra for (a) PEO/CNC and (b) PEO/CNF composites with various nanofiber contents..

with proton donors such as OH groups on CNCs and CNFs. Therefore, the change in the intensity ratio indicates that hydrogen bonding is established between PEO and CNCs (or CNFs). The perturbed C–O–C stretching subsequently causes the upshift of the CH_2 rocking peak.

DSC. Melting points (T_m), heat of fusion (ΔH_m), and crystallinity of all the samples are listed in Table 2. Neat PEO shows the highest values in all the three properties. The decreases in the polymer melting point and crystallinity after the addition of CNCs have been observed in poly(3-hydroxybutyrate-co-3-hydroxyvalerate)/CNC composites.[44] Similar results have also been reported for PEO/bacterial cellulose composites.[45] The reason is ascribed to the confinement effects of the nanoparticles, which hinders chain diffusion and folding at the crystal growth front and results in thin spherulite lamellar thickness.[44,45] The strong interactions between PEO and CNCs also thermodynamically contribute to the melting point depression of PEO.[45]

dx.doi.org/10.1021/am302624t | ACS Appl. Mater. Interfaces 2013, 5, 2999–3009

Table 2. Melting Characteristics of Neat PEO, PEO/CNCs, and PEO/CNFs

filler	content (wt %)	T_m (°C)	ΔH_m (J/g)[a]	crystallinity (%)
CNCs	0	71.2	154.5	82
	1	66.9	144.8	77
	4	66.8	145.9	78
	7	67.4	137.6	73
	10	69.2	134.3	71
CNFs	1	70.7	139.3	74
	4	66.8	149.3	79
	7	66.8	145.7	77
	10	69.9	130.3	69

[a] ΔH_m is based on PEO weight. Heat of fusion of 100% crystallinity PEO is 188 J/g.[46,47]

DMA. Loss tangents (tan δ) of PEO/CNCs and PEO/CNFs as a function of temperature are shown in Figures 8 and 9,

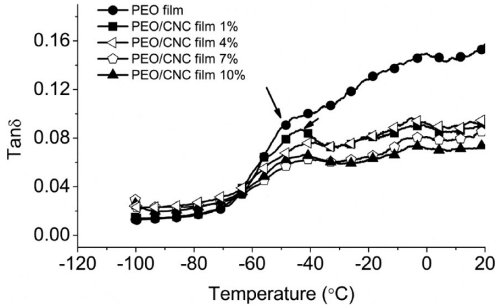

Figure 8. Tan δ of PEO/CNC nanocomposite films. The arrows point to the glass transition temperature (T_g) of pure PEO and the composites.

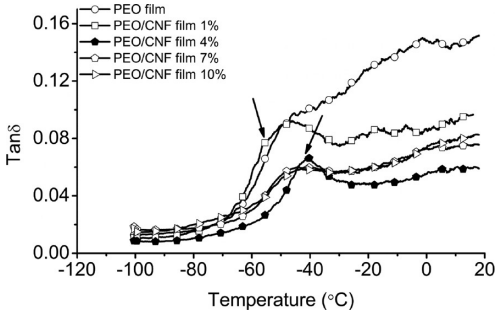

Figure 9. Tan δ of PEO/CNF nanocomposite films. The arrows point to the glass transition temperature (T_g) of pure PEO and the composites.

respectively. Pure PEO shows a peak at approximately −48 °C (intensity 0.09), which is attributed to its glass transition (Figure 8). The peak shifts to higher temperature and the peak intensity is reduced in all PEO/CNC nanocomposites. For instance, tan δ of PEO/CNCs at 4 wt % CNC loading peaks at approximately −-42 °C with an intensity of 0.07, which is 6 °C higher in temperature and 0.02 lower in tan δ compared to the pure PEO. A similar trend is also observed in PEO/CNF nanocompostites as shown in Figure 9. The PEO/CNFs comprising 4 wt % CNFs shows a tan δ peak of 0.06 at approximately −40°C, 0.03 lower in tan δ and 8°C higher in temperature than the pure PEO.

Tan δ is a measurement of viscoelastic damping of materials. The lower tan δ after the addition of CNCs or CNFs indicates that the composites become more elastic and less energy is dissipated during mechanical vibrations. This is due to the presence of CNCs or CNFs in the PEO matrix, which substantially restrains PEO chain segment movements through fiber-matrix interfacial actions and fiber−fiber interactions including physical fiber network structures at high fiber concentrations. The strong interfacial action (hydrogen bonding in this case as shown by FTIR results) is evident from the increases in PEO glass transition temperature. PEO chains are tethered to the surfaces of CNCs or CNFs through multiple hydrogen bonding sites and therefore more energy is required to achieve the same level of chain segment movement in the composites than in the pure PEO. A similar glass transition temperature (T_g) trend is also found in tunicin whiskers reinforced cross-linked polyether and lithium imade (LiTFSI) nanocomposites.[4] The larger shift in glass transition temperature and tan δ intensity demonstrated by PEO/CNFs indicates CNFs' bigger influence on the matrix than CNCs due to the former's stronger physical confinement effects[23] and more intensive hydrogen bonding interactions with the matrix. Glass transition temperature is also influenced by polymer crystallinity because the crystalline phase constrains mobility of the amorphous phase. However, the glass transition temperature increase in this study is not due to this, because the crystallinity of PEO is reduced after the addition of the cellulose nanoparticles.

Mechanical Reinforcing Effects of CNCs and CNFs. The nanoscale dimensions and high mechanical properties of CNCs and CNFs make them ideal for polymer reinforcement. Representative stress-strain curves for PEO/CNC and PEO/CNF composite films are plotted in Figures 10 and 11,

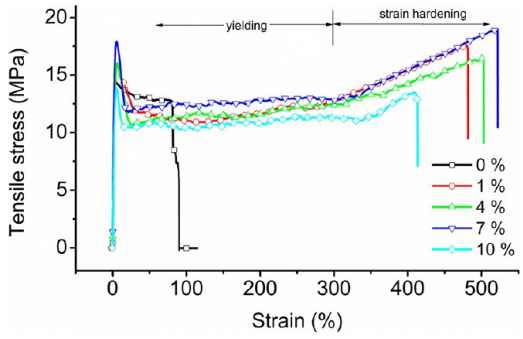

Figure 10. Tensile stress−strain curves for pure PEO and PEO/CNC films with 1, 4, 7, and 10% CNCs.

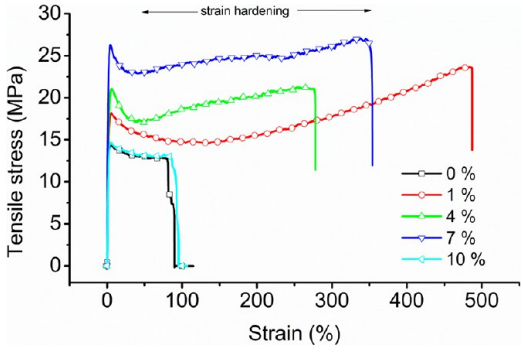

Figure 11. Tensile stress−strain curves for pure PEO and PEO/CNF films with 1, 4, 7, and 10% CNFs.

Table 3. Mechanical Properties of PEO/CNC and PEO/CNF Nanocomposite Films

filler	content (wt %)	Young's modulus (MPa)	yield strength (MPa)	stress-at-failure (MPa)	strain-at-failure (%)	toughness (kJ/m^3)
	0	760 ± 109	14.2 ± 0.9	12.8 ± 0.4	86 ± 14	1161 ± 20
CNCs	1	820 ± 195	15.9 ± 0.1	16.9 ± 2.1	495 ± 43	6157 ± 573
	4	895 ± 141	16.0 ± 0.8	16.2 ± 1.3	504 ± 34	6371 ± 618
	7	937 ± 150	17.6 ± 0.7	18.4 ± 2.0	526 ± 40	7083 ± 686
	10	758 ± 326	15.3 ± 0.2	13.8 ± 1.7	416 ± 43	4750 ± 705
CNFs	1	896 ± 99	17.7 ± 0.9	23.0 ± 1.0	491 ± 21	8267 ± 277
	4	994 ± 222	20.8 ± 0.7	20.9 ± 1.7	281 ± 56	5898 ± 539
	7	1727 ± 102	27.3 ± 0.9	26.9 ± 1.7	340 ± 62	9662 ± 112
	10	1235 ± 99	14.4 ± 0.5	16.4 ± 6.7	89 ± 55	1648 ± 300

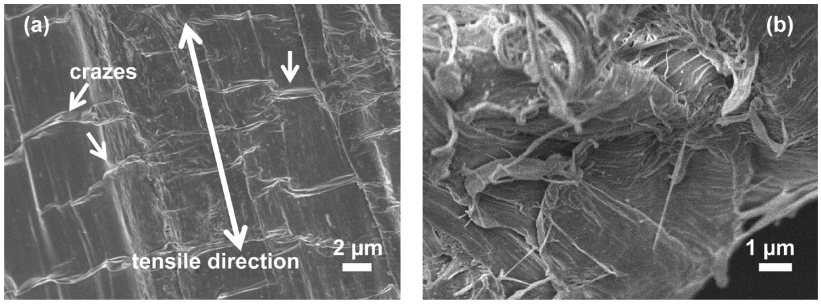

Figure 12. (a) Side and (b) fracture surfaces of pure PEO film.

respectively. Pure PEO shows a ductile fracture with a strain-at-failure of ca. 90%. The horizontal section of the curves in Figures 10 and 11 clearly demonstrates PEO's yielding behavior. After adding CNCs to the polymer, the strain range within which the yielding occurs is significantly expanded and an additional section of strain hardening (i.e., stress increased with strain) emerges (Figure 10). The addition of CNFs also leads to increases in strain-at-failure (smaller compared to CNCs) and the occurrence of strain hardening of the composites with various fiber concentrations (Figure 11). Most importantly, even at 1 wt % CNC or CNF content, the yielding and strain hardening are increased by approximately five-fold for both the PEO/CNC and PEO/CNF composites (Figures 10 and 11).

Young's modulus, yield strength, stress-at-failure, strain-at-failure, and fracture toughness of the samples were obtained from the curves and are summarized in Table 3. These mechanical properties exhibit a general trend: The properties increase and then decrease as nanocellulose content increases. The optimal content appears at 7% for both CNCs and CNFs. In table 3, the nanocomposite comprising 7 wt % CNCs shows a Young's modulus of ca. 937 MPa, yield strength of 17.6 MPa, stress-at-failure of 18.4 MPa, and strain-at-failure of 526%, which are 23, 124, 44, and 512% higher than those of pure PEO film respectively. The composite comprising 7 wt % CNFs shows even higher mechanical reinforcement (an increase of 127, 192, and 110% in modulus, yield strength, and stress-at-failure, respectively) but lower strain-at-failure increase (295%). Even at 1% substitution, the increases in these mechanical properties are significant. The increases in tensile strength and modulus are attributed to CNFs and CNCs' high mechanical properties and their strong interactions with the PEO matrix as demonstrated in FTIR and DMA results. PEO crystallinity is excluded as the possible reason for the enhancement because the crystallinity was reduced after the addition of the nanocellulose. The decreases in properties at high nanocellulose concentration (10%) are presumed to be caused by nanocellulose agglomerations that could be clearly seen in the TEM micrograph (Figure 5d).

It is also worth noting that in Figure 10 ,the strain hardening of all the PEO/CNC samples starts at ca. 300% strain, whereas in Figure 11 the hardening starts at much lower strains for PEO/CNF samples, with higher CNF concentration appearing to cause lower starts. Strain hardening occurred because CNCs or CNFs were expected to be increasingly aligned along the tensile direction during sample elongation and thus they were able to carry larger share of the load exerted on the samples. The stresses of the samples are therefore increased. Pure PEO does not show this behavior due to its lack of the reinforcing cellulose fibers. In addition, the large aspect ratio of CNFs and their entanglements, which assists in fiber-matrix and fiber–fiber load transfers,[45] also facilitates the early occurrence of the strain hardening of PEO/CNF samples.

The increases in strain-at-failure after the various substitution ratios of CNCs or CNFs are significant. In fiber reinforced polymer composites, the general trend is that strength and modulus of the composites are increased and strain-at-failure is decreased with fiber substitution. Reinforcement fibers are more rigid than their polymer matrixes and fracture at a lower strain compared to the matrixes. Their fractures not only create cracks throughout the composites but also shift the load that is originally carried by the fibers to the matrixes, which leads to swift matrix failure. Nanoparticles such as clay and calcium carbonate have been found to increase tensile strain of brittle polymer polylactic acid (PLA).[48,49] The main mechanism behind this toughening effect is attributed to interfacial debonding induced plastic deformation of the matrix polymer. Interfacial debonding releases strain constrains on the matrix polymer and lowers its plastic resistance, which allows plastic deformation to occur under suitable stress levels. In a study by Jiang et al, pure PLA showed a smooth fracture surface with little sign of plastic deformation whereas the nanoparticle filled PLA showed abundant PLA fibrils being pulled out from the fracture surface as a result of plastic deformation.[49] A similar

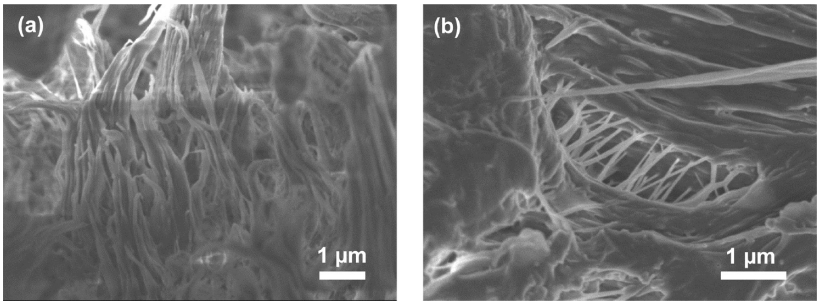

Figure 13. Fracture surfaces of PEO/CNC nanocomposite film with 7 wt % CNCs. The long arrow indicates the tensile load direction; the short arrows point to the crazes generated on the film surfaces after tensile tests.

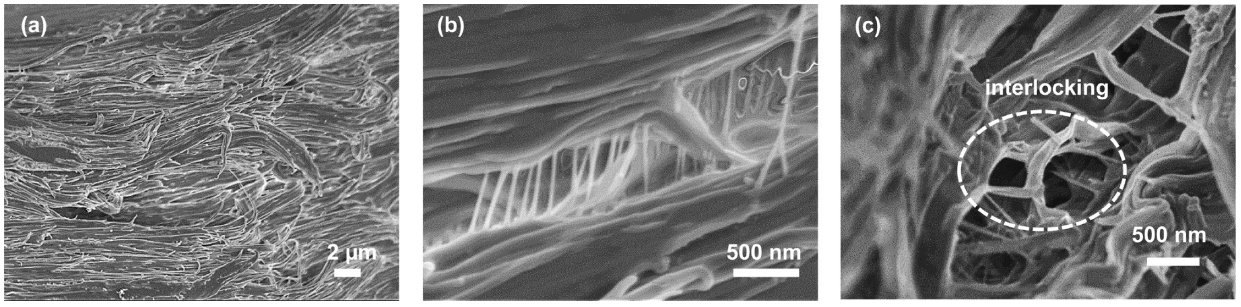

Figure 14. Fracture surfaces of PEO/CNF nanocomposite film with 7 wt % CNFs. Details circled by the ellipse indicate the interlocking between fibrils at the fracture surface.

contrast was observed between pure PEO and CNC or CNF filled PEO in this study as discussed in detail below.

Study of Fracture Surfaces. Tensile samples of pure PEO, PEO/CNCs, and PEO/CNFs changed from transparent to white materials with increasing strain during the tests. The white color is a result of light diffraction from the numerous crazes throughout the materials that are induced by the tensile stress. It is possible that CNCs and CNFs in the composites nucleate crazes at their surfaces through interfacial debonding. An example of the crazes on the side surface of pure PEO is shown in Figure 12a. The fracture surface of pure PEO shows signs of plastic deformation (e.g., rough and irregular surfaces, voids and dimples, and pull-out fibrils) (Figure 12b), which are in agreement with its ductile fracture as demonstrated by its stress-strain curve. The fracture surfaces of PEO/CNCs and PEO/CNFs exhibits intensive fibrillation as shown in Figures 13a and 14a, respetively. Nanofibrils of less than 50 nm diameter are evident in Figures 13b and 14b. These fibrils bridge the crazes throughout the samples, which contributes to the increased tensile strength and strain-at-failure. The composition of these nanofibrils remains unclear at this stage. They may be pure CNC (or CNF) bundles, pure PEO nanofibrils, or most likely CNC (or CNF) fibers (or bundles) with PEO sheaths. It appeared through FE-SEM observation that PEO/CNF samples showed a larger population of the bridging nanofibrils than did PEO/CNCs, which were possibly ascribed to CNFs' interfiber entanglements and much larger aspect ratio. Figure 15 illustrates the failure mechanisms of PEO when it is reinforced by CNCs and CNFs, respectively. Because of CNFs' larger lengths and higher flexibility, one CNF fibril could bridge a craze at multiple locations. The long lengths, network structures, and entanglements with connecting fibrils facilitates the formation of a large population of visible pullout nanofibrils and fibril interlocking (Figure 14c) on the fracture surfaces of PEO/CNFs.

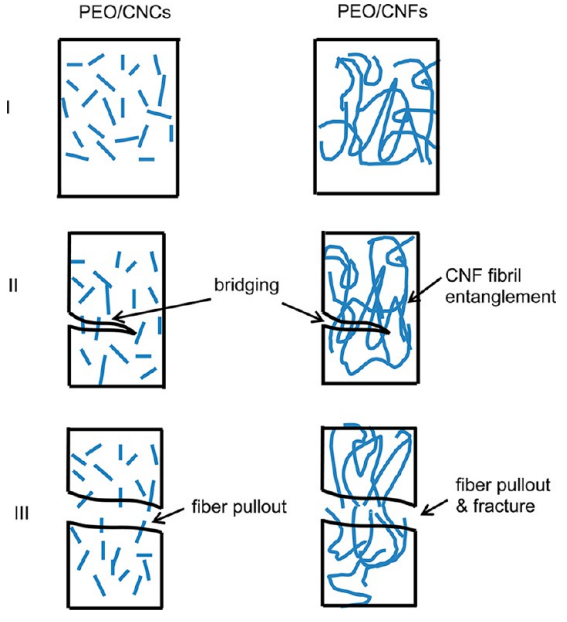

Figure 15. Illustrations of fracture mechanisms of PEO/CNC and PEO/CNF nanocomposites.

Siqueira et al. found increased modulus in PCL/CNC and PCL/CNF composites. The composites also showed decreases in strength and strain-at-failure after the addition of the nanofibers.[23] The authors ascribed the decreases to poor fiber–polymer interfacial adhesion and material defects due to fiber agglomerations. The increases in strength and strain-at-failure in this study resulted from the strong hydrogen bonding between PEO and the nanofibers and the relatively homogeneous dispersion of the fibers due to the strong interaction. Because of their increased strength and strain-at-failure, fracture toughness (the area below the stress–strain

curves) of the PEO/CNC and PEO/CNF nanocomposites comprising 7 wt % cellulose nanofibers were 610% and 832% larger, respectively, than that of pure PEO.

Mechanical Property Modeling. The Halpin-Kardos model and the Ouali model were used to simulate the moduli of the composites and their results were compared with the experimental values. The Halpin-Kardos model is a semi-empirical model for oriented short fiber composites[50]

$$E_{\parallel} = E_{\mathrm{m}}\frac{1 + \eta_{\parallel}\zeta\varphi_{\mathrm{f}}}{1 - \eta_{\parallel}\varphi_{\mathrm{f}}} \tag{3}$$

$$E_{\perp} = E_{\mathrm{m}}\frac{1 + 2\eta_{\perp}\varphi_{\mathrm{f}}}{1 - \eta_{\perp}\varphi_{\mathrm{f}}} \tag{4}$$

where,

$$\eta_{\parallel} = \frac{\frac{E_{\mathrm{f}}}{E_{\mathrm{m}}} - 1}{\frac{E_{\mathrm{f}}}{E_{\mathrm{m}}} + \zeta} \tag{5}$$

$$\eta_{\perp} = \frac{\frac{E_{\mathrm{f}}}{E_{\mathrm{m}}} - 1}{\frac{E_{\mathrm{f}}}{E_{\mathrm{m}}} + 2} \tag{6}$$

where $E_{\parallel}$ and $E_{\perp}$ are the longitudinal and transverse Young's modulus of the unidirectional composite, φ_f is the fiber volume fraction, E_- is the Young's modulus of the matrix, and $-_f$ is the modulus of the fiber. ζ is a shape factor dependent on fiber geometry and orientation. Different equations have been proposed to calculate ζ. Equation $\zeta = 2L/w$ is used for relatively short fibers such as CNCs.[51,52] Equation $\zeta = (0.5L/w)^{1.8}$ is proposed by Van Es for high aspect ratio fibers.[53] The modulus of a 3D randomly oriented composite (E_C) can be calculated based on the laminate theory[53]

$$E_{\mathrm{C}} = 0.184E_{\parallel} + 0.816E_{\perp} \tag{7}$$

The Ouali model is based on the percolation theory and is an extension of the phenomenological series-parallel model proposed by Takayanagi.[54−56] The Ouali model simulates polymer composites using three phases: matrix, percolating filler network, and non-percolating filler phase. The model is given by the following equation

$$E_{\mathrm{C}} = \frac{(1 - 2\psi + \psi\varphi_f)E_{\mathrm{m}}E_{\mathrm{f}} + (1 - \varphi_f)\psi{E_{\mathrm{f}}}^2}{(1 - \varphi_{\mathrm{f}})E_{\mathrm{f}} + (\varphi_{\mathrm{f}} - \psi)E_{\mathrm{m}}} \tag{8}$$

where the subscripts f and m refer to the filler and matrix phases, φ_{f} is the volume fraction of the filler, and E is the modulus. ψ denotes the volume fraction of the percolating filler network and is obtained from

$$\psi = 0\ \varphi_{\mathrm{f}} \le \varphi_{\mathrm{c}} \tag{9}$$

$$\psi = \varphi_{\mathrm{f}}\left(\frac{\varphi_{\mathrm{f}} - \varphi_{\mathrm{c}}}{1 - \varphi_{\mathrm{c}}}\right)^{\mathrm{b}}\varphi_{\mathrm{f}} > \varphi_{\mathrm{c}} \tag{10}$$

where b is the critical percolation exponent and a value of 0.4 is used for a three-dimensional network.[54,55] φ_{c} is the critical percolation threshold (volume fraction)[57]

$$\varphi_{\mathrm{c}} = 0.7/(L/w) \tag{11}$$

where L and w are the length and diameter of the filler, respectively. φ_c for CNCs and CNFs were calculated to be 8.75 and 1.35 vol% (12.7 and 1.8 wt %), respectively, when using PEO density of 1.2 g/cm^3 and CNC (or CNF) density of 1.59 g/cm^3. The modulus of PEO (E_{m}) was taken as 760 MPa based on the tensile results. The modulus of CNCs varies considerably (50−200 GPa) depending on the methods used to measure the property, types of cellulose (i.e. cellulose I or II), and the ratio between the two cellulose.[58−60] The modulus of CNFs is scarce in literature. A value of 78 ± 17 GPa was obtained for a single bacterial cellulose nanofibril using an atomic force microscopy tip bending method.[61] On the basis of the modulus of wood-derived CNF films (30 GPa),[62] values of 90 and 80 GPa can be obtained for a single nanofibril using the efficiency factors proposed by Cox[63] and Krenchel,[64] respectively. Most recently, using Raman spectroscopy the effective moduli of single fibrils of bacterial cellulose and CNFs were estimated to be ∼84 and ∼33 GPa, respectively.[65] In this study, a value of 145 GPa for CNCs[60] and 78 GPa for CNFs were used for theoretical modeling.

The experimental moduli of PEO/CNCs and PEO/CNFs and the simulation results based on the Halpin-Kardos and Ouali models are compared in Figure 16. Within the range of

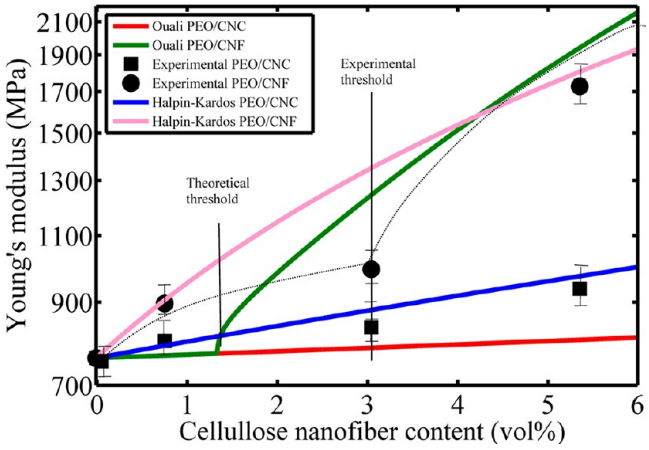

Figure 16. Young's modulus as a function of cellulose nanofiber content: experimental values vs. model predictions. $\zeta = 2L/w$ and $\zeta = (0.5L/w)^{1.8}$ are used for PEO/CNCs and PEO/CNFs, respectively, in the Halpin−Kardos model.

experimental nanofiber contents, the Halpin-Kardos model gives a close prediction of the moduli of the PEO/CNC composites. The Ouali model on the other hand underpredicts the moduli. For the PEO/CNF composites, both models predict the moduli with reasonable accuracy. The percolation model appeared to be able to capture the modulus jump after the CNF content exceeded φ_c.[52] However, the theoretical φ_{c} that depends on L and w of CNFs deviated from its experimental value (Figure 16). This are probably attributed to two main errors. First, the values of L and w are estimated based on the CNFs dispersed in water. The CNFs in the PEO matrix could have more severe aggregations than in water because of the PEO solution's higher viscosity and weaker hydrogen bonding with the fiber. Second, the mechanical dispersion steps used to mix PEO and CNFs could also change the sizes of CNFs. Both errors could result in a reduced CNF aspect ratio and thus increase φ_c as demonstrated by the experimental moduli. Admittedly, a larger fiber content range is

required to better compare the accuracy of the two models, especially for the results of the PEO/CNF composites. Nevertheless, the range is limited within 10 wt % in this study because fiber agglomerations occur when the fiber content exceeds 7 wt %.

The Halpin−Kardos model is based on self-consistent theory by considering a single fiber encased in a cylindrical shell of matrix.[49] Interactions between fibers are not considered in this model. Takayanagi developed a phenomenological model to calculate the modulus of a multi-phase polymer system by symbolizing the system with serial/parallel phases. Ouali extended the Takayanagi model by adding a percolating filler network phase (in parallel) to a series part comprising a matrix phase and a nonpercolating filler phase.[54] When the volume ratio of filler exceeds its percolation threshold, filler−filler interactions are taken into account through the percolating filler phase in Ouali's model. Both Halpin−Kardos and Ouali models assume perfect filler−matrix bonding. Our results show that the Halpin−Kardos model is accurate for short fiber composites (i.e., PEO/CNCs) whose filler−filler interactions are negligible (i.e., filler concentration below percolation threshold). It fails to capture the modulus jump in long fiber composites (i.e., PEO/CNFs) above the filler percolation threshold because filler−filler interactions are not considered in this model. In contrast, the Ouali model predicts the trend of the modulus of PEO/CNFs. One may expect that the Ouali model provides higher prediction accuracy than does the Halpin−Kardos model when the fiber concentration exceeds the tested range. The difference in the prediction results highlights the importance of filler−filler interactions to the properties of the composites containing high concentrations of fillers.

In Figure 16, both model predictions and experimental values show that CNFs lead to higher composite moduli than do CNCs at the same fiber contents. This is mainly due to CNFs' larger aspect ratio as evidenced by the model equations. The extensive CNF fiber entanglements and percolation networks which are cemented together through hydrogen bonds and mechanical interlocking in the PEO matrix also contributes to the high moduli. These results have important implications in developing new polymer composites. The high strength and modulus of short fibers are often underused because their aspect ratios are too small to enable a full-scale stress transfer from the matrixes to the fibers.[66] As a result, long fibers with relatively low strength and modulus can outperform short high-strength fibers in reinforcing composites. Moreover, long fibers reach percolation at low fiber contents. The fiber−fiber interactions caused by the percolation contribute to further improvement in the mechanic properties of composites. Therefore in searching for the right fibers for reinforcement, fiber aspect ratio should outweigh fiber strength as a more important consideration factor. This priority also has its economic benefits because low strength fibers are generally less costly.

CONCLUSIONS

A systematic comparison between CNCs and CNFs was made in this study with focus on their microstructures, interfacial bonding with the PEO matrix, and the resulting effects on the dynamic and mechanical properties of the PEO/CNC and PEO/CNF nanocomposites. The nanocomposites containing up to 10 wt % nanocellulose were prepared by simple solution casting. The maximum strength, modulus and fracture toughness of the composites were found to occur at 7 wt % fiber content for both CNCs and CNFs. The increases were attributed to strong fiber-matrix interfacial bonding and large aspect ratios of the fibers. CNFs led to higher strength and modulus than did CNCs at the same fiber concentration due to CNFs' much larger aspect ratio and their percolation networks. The entanglements and percolation of CNFs also resulted in their higher probability of fiber agglomeration compared to CNCs, which caused lower strain-at-failure for PEO/CNF composites. The moduli of the composites were simulated using two models and their accuracies were compared. The Ouali model was found to be more accurate for PEO/CNF composites, whereas the Halpin-Kardos model was more suitable for PEO/CNC composites. The results from this comparative study are important for proper selection of nanocellulose materials as reinforcing agents in polymer composites.

AUTHOR INFORMATION

Corresponding Author

*E-mail: long.jiang@ndsu.edu. Tel: +1 (701) 231 9512. Fax: +1 (701) 231 8913.

Notes

The authors declare no competing financial interest.

ACKNOWLEDGMENTS

The authors thank Prof. Chad Ulven, Dr. Shanshan Huo, Jessica L. Lattimer and Tingting Zhou for their assistance with the DMA tests. The authors are also grateful to Scott A. Payne and Moore Jayma for performing SEM and TEM. QianQian Wang, a visiting student at the USDA Forest Service, Forest Products lab, is also appreciated for producing the CNC and CNF samples. Financial support from North Dakota EPSCoR is greatly appreciated.

REFERENCES

(1) Siqueira, G.; Bras, J.; Dufresne, A. *Polymers* **2010**, *2*, 728−765.
(2) Habibi, Y.; Lucia, L. A.; Rojas, O. J. *Chem. Rev.* **2010**, *110*, 3479−3500.
(3) Wang, Q. Q.; Zhu, J. Y.; Reiner, R. S.; Verrill, S. P.; Baxa, U.; McNeil, S. E. *Cellulose* **2012**, *19*, 2033−2047.
(4) Samir, M. A. S. A.; Alloin, F.; Paillet, M.; Dufresne, A. *Macromolecules* **2004**, *37*, 4313−4316.
(5) Samir, A.; Alloin, F.; Sanchez, J.; Kissi, N. E.; Dufresne, A. *Macromolecules* **2004**, *37*, 1386−1393.
(6) Park, W. I.; Kang, M.; Kim, H. S.; Jin, H. J. *Macromol. Symp.* **2007**, *249-250*, 289−294.
(7) Cao, X.; Chen, Y.; Chang, P. R.; Muir, A. D.; Falk, G. *Express Polym. Lett.* **2008**, *2*, 502−510.
(8) Qi, H.; Cai, J.; Zhang, L.; Kuga, S. *Biomacromolecules* **2009**, *10*, 1597−1602.
(9) Peresin, M. S.; Habibi, Y.; Zoppe, J. O.; Pawlak, J. J.; Rojas, O. J. *Biomacromolecules* **2010**, *11*, 674−681.
(10) Cao, X.; Dong, H.; Li, C. M. *Biomacromolecules* **2007**, *8*, 899−904.
(11) Siqueira, G.; Abdillahi, H.; Bras, J.; Dufresne, A. *Cellulose* **2009**, *17*, 289−298.
(12) Guhados, G.; Wan, W.; Hutter, J. L. *Langmuir* **2005**, *21*, 6642−6646.
(13) Henriksson, M.; Berglund, L. A.; Isaksson, P.; Lindström, T.; Nishino, T. *Biomacromolecules* **2008**, *9*, 1579−1585.
(14) Iwamoto, S.; Nakagaito, A. N.; Yano, H. *Appl. Phys. A* **2007**, *89*, 461−466.
(15) Wang, Q. Q.; Zhu, J. Y.; Gleisner, R.; Kuster, T. A.; Baxa, U.; McNeil, S. E. *Cellulose* **2012**, *19*, 1631−1643.
(16) Chinga-Carrasco, G. *Nanoscale Res. Lett.* **2011**, *6*, 417.

(17) Nakagaito, A. N.; Yano, H. *Cellulose* **2008**, *15*, 555−559.
(18) Seydibeyoğlu, M. O.; Oksman, K. *Compos. Sci. Technol.* **2008**, *68*, 908−914.
(19) Iwatake, a; Nogi, M.; Yano, H. *Compos. Sci.Technol.* **2008**, *68*, 2103−2106.
(20) Wu, Q.; Henriksson, M.; Liu, X.; Berglund, L. *A. Biomacromolecules* **2007**, *8*, 3687−3692.
(21) Cheng, Q.; Wang, S.; Rials, T. G. *Compos. Part A* **2009**, *40*, 218−224.
(22) Choi, Y.; Simonsen, J. *J. Nanosci. Nanotechnol.* **2006**, *6*, 633−639.
(23) Siqueira, G.; Bras, J.; Dufresne, A. *Biomacromolecules* **2009**, *10*, 425−432.
(24) Johnson, R. K.; Zink-Sharp, A.; Renneckar, S. H.; Glasser, W. G. *Cellulose* **2008**, *16*, 227−238.
(25) Lee, K. Y.; Tammelin, T.; Schulfter, K.; Kiiskinen, H.; Samela, J.; Bismarck, A. *ACS Appl. Mater. Interfaces* **2012**, *4*, 4078−4086.
(26) Liu, D.; Chen, X.; Yue, Y.; Chen, M.; Wu, Q. *Carbohyd. Polym.* **2011**, *84*, 316−322.
(27) Asghar, A.; Samad, Y. A.; Hashaikeh, R. *J. Appl. Polym. Sci.* **2012**, 125.
(28) Pielichowska, K.; Pielichowski, K. *Polym. Adv. Technol.* **2011**, *22*, 1633−1641.
(29) Wang, Q. Q.; Zhu, J. Y.; Reiner, R. S.; Verrill, S. P.; Baxa, U.; McNeil, S. E. *Cellulose* **2012**, *19*, 2033−2047.
(30) Scherrer, P. *Göttinger Nachr. Ges.* **1918**, *26*, 98−100.
(31) Park, S.; Baker, J. O.; Himmel, M. E.; Parilla, P. A.; Johnson, D. K. *Biotechnol. Biofuels* **2010**, 3−10.
(32) Segal, L.; Creely, J. J.; Martin, A. E.; Conrad, C. M. *Tex. Res. J.* **1959**, *29*, 786−794.
(33) Li, R.; Fei, J.; Cai, Y.; Li, Y.; Feng, J.; Yao, J. *Carbohyd. Polym.* **2009**, *76*, 94−99.
(34) Oudiani, A. E.; Chaabouni, Y.; Msahli, S.; Sakli, F. *Carbohyd. Polym.* **2011**, *86*, 1221−1229.
(35) Brown, R. D.; Jurasek, L. *Hydrolysis of Cellulose: Mechanisms of Enzymatic and Acid Catalysis*; The Maple Press Co.: York, PA, 1979.
(36) Moon, R. J.; Martini, A.; Nairn, J.; Simonsen, J.; Youngblood, J. *Chem. Soc. Rev.* **2011**, *40*, 3941−3994.
(37) Elazzouzi-Hafraoui, S.; Nishiyama, Y.; Putaux, J.-L.; Heux, L.; Dubreuil, F.; Rochas, C. *Biomacromolecules* **2008**, *9*, 57−65.
(38) Kadla, J. F.; Kubo, S. *Macromolecules* **2003**, *36*, 7803−7811.
(39) Kondo, T.; Sawatari, C.; Gray, D. G. *Macromolecules* **1994**, *27*, 210−215.
(40) Su, Y. L.; Wang, J.; Liu, H. Z. *J. Colloid Interface Sci.* **2002**, *251*, 417−423.
(41) Kakade, M. V; Givens, S.; Gardner, K.; Lee, K. H.; Chase, D. B.; Rabolt, J. F. *J. Am. Chem. Soc.* **2007**, *129*, 2777−2782.
(42) Xu, X.; Jiang, L.; Zhou, Z.; Wu, X.; Wang, Y. *ACS Appl. Mater. Interfaces* **2012**, *4*, 4331−4337.
(43) Pereira, R. P.; Rocco, A. M.; Bielschowsky, C. E. *Macromol. Symp.* **2004**, *108*, 12677−12684.
(44) Brown, E. E.; Laborie, M. G. *Biomacromolecules* **2007**, *8*, 3074−3081.
(45) Ten, E.; Jiang, L.; Wolcott, M. P. *Carbohyd. Polym.* **2012**, *90*, 541−550.
(46) Cimmino, S.; Pace, E. *Die Makromol. Chem.* **2003**, *191*, 2447−2454.
(47) Rocco, A. M.; Pereira, R. P.; Felisberti, M. I. *Polymer* **2001**, *42*, 5199−5205.
(48) Ozkoc, G.; Kemaloglu, S. *J. Appl. Polym. Sci.* **2009**, *114*, 2481−2487.
(49) Jiang, L.; Zhang, J.; Wolcott, M. P. *Polymer* **2007**, *48*, 7632−7644.
(50) Halpin, J. C.; Kardos, J. L. *J. Appl. Phys.* **1972**, *43*, 2235−2241.
(51) Dalmas, F.; Cavaillé, J. Y.; Gauthier, C.; Chazeau, L.; Dendievel, R. *Compos. Sci. Technol.* **2007**, *67*, 829−839.
(52) Capadona, J. R.; Shanmuganathan, K.; Tyler, D. J.; Rowan, S. J.; Weder, C. *Science* **2008**, *319*, 1370−1374.
(53) Van Es, M. A.; Xiqiao, F.; van Turnhout, J.; van der Giessen, E. In *Specialty Polymer Additives: Principles and Applications*; Al-Malaika, S., Golovoy, A. W., Wilkie, C. A., Ed.; John Wiley & Son: Hoboken, NJ, 2001; pp 391−414.
(54) Ouali, N.; Cavaille, J. Y.; Perez, J. *Plast. Rubber Compos. Process. Appl.* **1991**, *16*, 55−60.
(55) Takayanagi, M.; Uemura, S.; Minami, S. *J. Polym. Sci., Part C: Polym. Symp.* **1964**, *5*, 113.
(56) Favier, V.; Chanzy, H.; Cavaille, J. Y. *Macromolecules* **1996**, *28*, 6365−6367.
(57) Fourier, J.; Canova, G. R.; Shrivastava, S. C.; Cavaille, J. Y. *Polym. Eng. Sci.* **1997**, *37*, 1732−1739.
(58) Rusli, R.; Eichhorn, S. J. *Appl. Phys. Lett.* **2008**, *93*, 033111.
(59) Lahiji, R. R.; Xu, X.; Reifenberger, R.; Raman, A.; Rudie, A.; Moon, R. J. *Langmuir* **2010**, *26*, 4480−8.
(60) Sturcová, A.; Davies, G. R.; Eichhorn, S. J. *Biomacromolecules* **2005**, *6*, 1055−1061.
(61) Guhados, G.; Wan, W.; Hutter, J. L. *Langmuir* **2005**, *21*, 6642−6646.
(62) Hult, E. L.; Iotti, M.; Lenes, M. *Cellulose* **2010**, *17*, 575−586.
(63) Cox, H. L. *Br. J. Appl. Phys.* **1952**, *3*, 72−79.
(64) Krenchel, H. *Fibre Reinforcement: Theoretical and Practical Investigations of the Elasticity and Strength of Fibre-Reinforced Materials*; Akademisk Forlag: Copenhagen, Denmark, 1964; pp 11−20.
(65) Tanpichai, S.; Quero, F.; Nogi, M.; Yano, H.; Young, R. J.; Lindstro, T.; Sampson, W. W.; Eichhorn, S. J. *Biomacromolecules* **2012**, *13*, 1340−1349.
(66) Agarwal, B. D.; Broutman, L. J.; Chandrashekhara, K. *Analysis and Performance of Fiber Composites*, 3rd ed.; Wiley: New York, 2006; pp 8−9.